nature communications

Article

https://doi.org/10.1038/s41467-026-71912-z

Atomic-scale quantification of individual oxygen vacancies and structural evolution in valence change memristors

Received: 24 September 2025

Accepted: 1 April 2026

Published online: 18 April 2026

Check for updates

Zhengzhou Wang[1,2,7], Weixiao Lin[1,2,7], Yongqiang Li[1,2], Meiyan Wang[1,2], Anan Guo[1,2], Hao Luo[1,2], Xiahan Sang[1,2], Lei Jin[3], Cheng Chen[1], Wen Zhao[4], Heguang Liu[5], Rafal E. Dunin-Borkowski[3] ✉ & Jinsong Wu[1,2,6] ✉

Elucidating the valence change mechanism in oxides memristors remains challenging due to subtle oxygen vacancy migration. Here, we quantify individual oxygen vacancies and observe their dynamic evolution during resistive switching using in-situ transmission electron microscopy. In $SrNbO_{3.4}$, when fewer than 3 oxygen vacancies per unit formula form, they distribute uniformly. This solid-solution structure ensures reversible oxygen vacancy creation and annihilation. Conversely, excessive vacancies (≥ 3) trigger a defective structure that degrades cycling stability, while further oxygen loss induces an orthorhombic-to-cubic phase transition. If this conductive cubic phase forms a filament, the device fails permanently. By adding a thin amorphous $SrNbO_3$ layer, we suppress interfacial oxygen loss and significantly enhance switching reversibility. This atomic-scale visualization provides direct insight into valence-change electroresistance mechanisms that are distinct from conventional filament formation models.

Resistance random-access memory, with its great potential of high density, high speed, and non-volatile, stands as one of the most promising candidates for next-generation memory technology[1–5]. Many materials have shown resistance switching properties, such as TaO_x[6], HfO_x[7], $SrTiO_3$[8–12], $In_{4/3}P_2S_6$[13], MoS_2[14], BiOI[15], $Cs_2AgSbBr_6$[16]. In particular, transition metal oxides play an important role in this emerging field[17–19], providing opportunities for further integration of potential versatility into a single device.

Oxygen vacancy plays a crucial role in the resistance switch of valence change memory devices, with large number of oxides with resistive change relying on the migration of oxygen vacancies to form conductive filamentary paths[2,12,20–22]. However, due to the lack of a direct method of observing individual oxygen vacancies, the kinetics and dynamical mechanism on the generation and migration of oxygen vacancies, and thus their role in the resistance switching, remains largely unclear. With the recent development of in-situ high-resolution scanning and transmission electron microscopy (S/TEM) techniques[23–26], it becomes possible to direct visualize the microstructural evolutions during resistive switching processes. Still, directly imaging individual oxygen vacancies by S/TEM remains challenging since the scattering of such a single vacancy by high energy electron is quite weak. Owing to the importance of oxygen vacancies to the resistive mechanism, it is essential to develop methods for quantifying individual oxygen vacancies.

Strontium niobate has been studied as a functional material for nanodevice with valence change mechanism[27]. It has formula $Sr_nNb_nO_{3n+2}$, where n stands for the number of octahedral layers of the NbO_6 octahedral atomic module, and is a class of compounds with a layered perovskite structure (Supplementary Fig. 1). The crystal structure and physical properties of such compounds are strongly

[1]State Key Laboratory of Advanced Technology for Materials Synthesis and Processing, Wuhan University of Technology, Wuhan, China. [2]Hubei Longzhong Laboratory, Wuhan University of Technology (Xiangyang Demonstration Zone), Xiangyang, China. [3]Ernst Ruska-Centre for Microscopy and Spectroscopy with Electrons (ER-C), Forschungszentrum Jülich GmbH, Jülich, Germany. [4]School of Materials Science and Engineering, China University of Petroleum (East China), Qingdao, China. [5]School of Materials Science and Engineering, Xi'an University of Technology, Xi'an, China. [6]Yangtze Laboratory, Wuhan, China. [7]These authors contributed equally: Zhengzhou Wang, Weixiao Lin. ✉e-mail: r.dunin-borkowski@fz-juelich.de; wujs@whut.edu.cn

relied on their oxygen content, and subtle variations in oxygen content can regulate their atomic structure and physical properties[28]. For example, perovskite $SrNbO_3$ is a metallic oxide with the electronic structure of Nb-4d[29]. However, oxygen-rich compounds such as $Sr_5Nb_5O_{17}$ (*i.e.* $SrNbO_{3.4}$) and $Sr_2Nb_2O_7$ (*i.e.* $SrNbO_{3.5}$), obtained by interspersing the perovskite lattice of $SrNbO_3$ with additional oxygen planes exhibit quasi-one-dimensional conductivity (Supplementary Fig. 2) and ferroelectric properties[30,31]. The conductive properties of the compound originate from the Nb^{4+} ion, and the NbO_6 octahedron within the conductive layer are all undistorted regular octahedron[32]. Given the complex structural variation modulated by oxygen content, the dynamic evolution of oxygen vacancies in strontium niobate during resistance switching remains unresolved.

In this work, using $SrNbO_{3.4}$ as the model oxide, Nb:$SrTiO_3$/$SrNbO_{3.4}$/W (NSTO/SNO/W) memristor devices are designed and fabricated, enabling correlation between microstructural evolution and resistive properties. In SNO-type oxides, the resistance sharply decreases (SET process) as oxygen anions migrate out of the lattice under an applied electric bias. During the RESET process under reverse bias, these anions reversibly reintegrate into the structure, restoring the high-resistance state (HRS) and ensuring robust cycling stability. However, the low-resistance state (LRS) of SNO immediately post-SET is inherently unstable. For instance, the resistance spontaneously increases once the SET voltage is removed, even before the reverse RESET voltage is applied. This instability poses a significant challenge for maintaining the programmed state in practical device operation. To investigate the origin of cycling instability, a quantitative STEM technique was developed to image individual oxygen vacancies and track structural evolution during resistive switching. By analyzing Sr column intensity deviations, we precisely quantified local oxygen vacancies and observed quantized oxygen vacancy creation and migration. Our findings reveal that reversible oxygen vacancy migration is achievable only when fewer than 3 vacancies per structural unit formula are generated. Under this threshold, the orthorhombic lattice remains intact by forming a uniform 'solid-solution' structure, where vacancies distribute homogeneously to minimize strain. However, exceeding 3 vacancies per structural unit formula triggers heterogeneous nucleation of a defective structure at the oxygen-depleted interface. The defective structure establishes low-energy pathways for rapid oxygen-ion diffusion and resists structural recovery during RESET. Consequently, the low-resistance state post-SET becomes unstable, degrading cycling performance. Furthermore, at a high voltage, device failure occurs when a defective structure grows, forming conductive filaments that prevent RESET *(i.e.*, inability to restore high resistance). We then demonstrate that incorporating a reliable oxygen reservoir—rather than an oxygen-blocking layer—is critical to enabling reversible oxygen vacancy migration in SNO-type oxides. We then fabricated an NSTO/C-SNO/A-SNO/W structure (C-SNO: crystalline $SrNbO_{3.4}$; A-SNO: amorphous $SrNbO_3$) by incorporating an amorphous SNO oxygen reservoir layer adjacent to the top electrode, showing significantly enhanced cycling stability.

Results and discussion

The microstructure and performance of the memristors

The microstructure of the device was characterized by cross-sectional STEM and energy dispersive X-ray spectroscopy (EDS) elemental mapping. The three-layer structure of NSTO/SNO/W is confirmed with two clear interfaces (Fig. 1a). From the atomic resolution high-angle annular dark field (HAADF) STEM image of the SNO layer (Fig. 1b) and its fast Fourier transform (FFT) pattern (Fig. 1c), it is identified that SNO has an orthogonal structure with a lattice parameter of $a = 32.45$ Å, $b = 5.67$ Å, $c = 3.99$ Å and space group *Pnn*2, in which the NbO_6 octahedra are chainlike connected along the crystallographic *b* axis. Figure 1d shows the simulated selected area electron diffraction (SAED) pattern along the [001] zone axis of the orthorhombic SNO phase, which agrees well with the experimental results. The SNO film has a good epitaxial relationship with the substrate NSTO (Supplementary Fig. 3). The integrated differential phase contrast (iDPC)-STEM image of the SNO film is shown in Fig. 1e, where oxygen columns are clearly identified (although it is still difficult to distinguish any possible oxygen vacancies). The Sr and Nb columns can be clearly identified by the atomically resolved EDS elemental mapping images (Fig. 1f). The insulating layer with metal/O ratio of 1:4 (which is the oxygen-rich layer) and the conducting layer with metal/O ratio of 1:3 are labeled in Fig. 1e.

The memristive characteristics of NSTO/SNO/W devices are tested. The structure of the fabricated memristor is shown in Supplementary Fig. 4a, and the current-voltage (I-V) characteristics of an SNO memristor during 100 cycles are shown in Supplementary Fig. 4b, demonstrating a bipolar switching characteristic. The memristor follows basically oxygen vacancy modulated valence change mechanism, which resistive change is mainly determined by electroresistance property under the applied voltage (Supplementary Fig. 5). The W/SNO interface forms an ohmic contact due to the lower work function of W (4.91 eV) compared to the SNO (5.29 eV) (Supplementary Fig. 6), which eliminates the interfacial rectifying barrier and enables the I-V characteristics to directly reflect bulk conductivity modulation by oxygen vacancy migration. The I-V measurement confirmed that the device current is proportional to the electrode area (as shown in the Supplementary Fig. 7), which is consistent with the non-filamentary switch. However, there are significant variations in the I-V curves, indicating poor cycling stability. Supplementary Fig. 4c shows the SET/RESET voltage histogram with a narrow distribution, where the corresponding standard deviations are 0.083 V and 0.053 V, respectively. The unstable switching behavior between LRS and HRS is shown in Supplementary Fig. 4d, e, where the HRS/LRS ratio changes from 26:1 to 7:1, and the current in LRS decreases by 92.8%, respectively. The SET and RESET operating power of the SNO memristor is calculated to be 0.1 nW and 5.3 nW, respectively, which is comparable to other advanced technologies. For comparison, the power consumption based on SNO films and other bipolar memristors is summarized in Supplementary Fig. 4f.

Method of oxygen vacancies quantification

Combined with density functional theory (DFT) calculations, a STEM-based imaging method to quantify individual oxygen vacancies is established, and applied to interpret the in-situ biasing S/TEM results to explore the resistive switching mechanisms. The experimental setup for in-situ observation is illustrated in Supplementary Fig. 8, with which dynamic structural evolutions can be monitored while there is a resistance change. A high-resolution HAADF-STEM image of the SNO thin film in its original HRS (at 0 V) is shown in Fig. 2a. In both the conducting and insulating layers, Sr and Nb atoms are alternately distributed, as evidenced by their intensity line profile along the [100] direction (Fig. 2b, c). When the applied voltage is switched from 0 to −8 V, the measured resistance of the sample decreases by two orders of magnitude, as shown in Supplementary Fig. 9. The corresponding HAADF-STEM image of the SNO thin film in its LRS (at −8 V) is shown in Fig. 2d. In the insulating (and oxygen-rich) layer, the distribution of Sr has a clear deviation as shown in Fig. 2e, while in the conducting layer, deviation in the atomic structure can be hardly observed (Fig. 2f). From HAADF (Supplementary Fig. 10a), iDPC (Fig. 1e), and simulated HAADF and ABF images (Supplementary Fig. 10b–e) without oxygen vacancies and with one oxygen vacancy, it can be demonstrated that the splitting of the atomic column is the displacement of the Sr atoms, rather than the displacement of the oxygen atoms. The control experiments of electron beam irradiation confirmed that under the same imaging conditions as the in-situ bias voltage experiment, the structure of the material remained stable during a continuous 5-minute electron beam irradiation (Supplementary Movie 1, Supplementary Fig. 11, and

https://doi.org/10.1038/s41467-026-71912-z

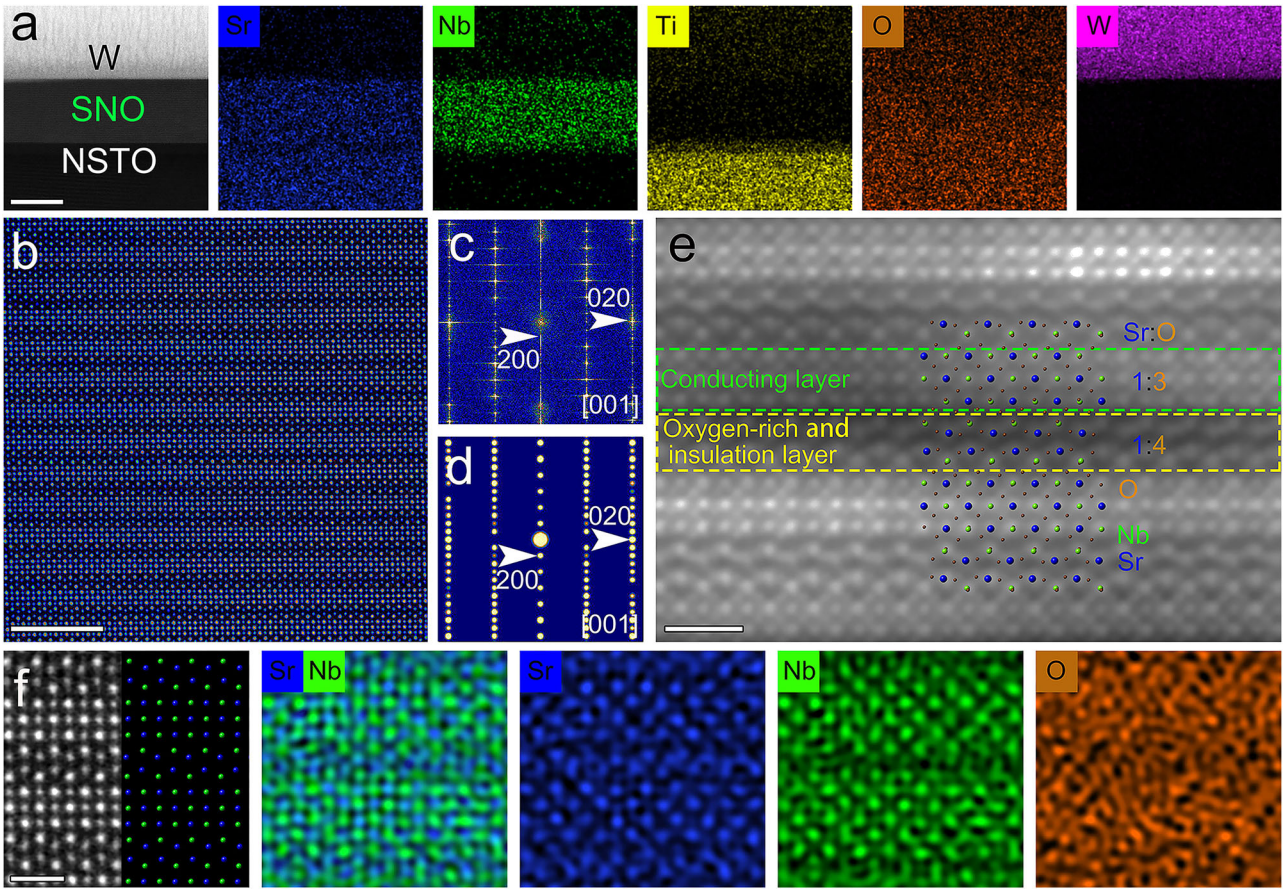

Fig. 1 | Characterization of cross section structure in NSTO/SNO/W devices. **a** The EDS elemental mapping of the cross-section in NSTO/SNO/W device. Scale bar = 50 nm. **b** The high-resolution HAADF image in the [001] zone axis of SNO. Scale bar = 5 nm. **c, d** The FFT image of HAADF in (**b**) and the corresponding simulated SAED image. **e** The SNO atomically resolved iDPC-STEM image. The illustration shows an atomic model in the [001] zone axis of SNO (Nb: green atom, Sr: blue atom, O: brown atom). Scale bar = 1 nm. **f** The atomic resolution EDS elemental mapping of SNO. Scale bar = 1 nm.

Supplementary Table 1), and there were no signs of oxygen vacancies formation. Thus, it was confirmed that the observed effect was driven by the electric field rather than electron beam damage[33,34]. From the line profiles in the oxygen-rich layer (Fig. 2e), it is evident that the intensity of Sr decreases and splits, while the intensity of Nb remains nearly unchanged. There are additional one or two Sr peaks that appeared near the original Sr atom positions. The variation of local oxygen content can be measured by electron energy loss spectroscopy (EELS). As shown in Supplementary Fig. 12b, the O − K edges are characterized mainly by two edge onsets (denoted a and b peaks). The peak intensity ratio a/b should qualitatively reflect the oxygen content. The intensity ratio a/b (0.81) of the Sr deviation region is significantly smaller than a/b (0.88) of the non-Sr deviation region. This indicates that the oxygen content in the Sr deviation region decreases. By measuring the distance of Sr deviation as represented in the line profiles in several regions outlined in the HAADF-STEM image taken at −8 V (Fig. 3a–h), it is found that the distances of Sr deviation exhibit several discrete values, *i.e.* 0.4, 0.7 and 1.0 Å. Combined with DFT calculations, it is identified that the quantized Sr shift corresponds to the generation of 1, 2, and 3 oxygen vacancies, respectively, in the oxygen-rich layer. The formation energy of oxygen vacancy in SNO is initially calculated, as shown in Supplementary Fig. 13a, indicating that the oxygen vacancy firstly forms at the two positions (V_{O1} or V_{O2}). The Sr_0 atom will shift to the nearby Sr_1 position when 1 oxygen atom (at V_{O1} position) is lost, and to Sr_2 position when 2 oxygen atoms are lost (both V_{O1} and V_{O2} positions), as shown in Supplementary Fig. 13b, c. A larger shift (of Sr_0) is found when 3 oxygen atoms are lost (Supplementary Fig. 13d). The lost oxygen is mainly from the oxygen-rich layer (*i.e.* the zigzag insulating layer, as shown in the Supplementary Fig. 2). Figure 3i shows the deviation distance of Sr atom along the [100] direction due to different oxygen vacancy concentration, as calculated by DFT. It is further confirmed that the distance of Sr shift is linearly correlated with the concentration of oxygen vacancy (Supplementary Fig. 14), *i.e.* the distance of the Sr shift increases by about 0.3 Å for each additional oxygen vacancy per formula. Thus, the oxygen vacancy in each structure formula can be quantified by the distance of the Sr shift. Supplementary Fig. 15 is the strain maps of the sample before (0 V) and after applying bias (−8 V) calculated by geometric phase analysis, indicating that elastic strain is generated during the generation of oxygen vacancies, validating the method of quantifying oxygen vacancy.

The structural evolution with increase of oxygen vacancies

With the established method, it is found that when the number of oxygen vacancies is fewer than 3 per structural unit formula (Supplementary Fig. 16), a solid-solution-like structure containing oxygen vacancies forms, retaining robust reversibility in generation and annihilation of oxygen vacancies in first few circles. By monitoring the Sr shift, the regions with injected oxygen vacancies (caused by the applied voltage of −8 V) can be identified, as shown in Supplementary Fig. 17. Unlike a filamentary distribution (in most of the previous studies), the regions with oxygen vacancies are uniformly distributed across the entire SNO film (Supplementary Fig. 17). By measuring the distance of Sr deviation, it is found that these regions predominantly contain either 1 or 2 oxygen vacancies per structural unit formula, with nearly equal probabilities for each case (Supplementary Fig. 14b). The

https://doi.org/10.1038/s41467-026-71912-z

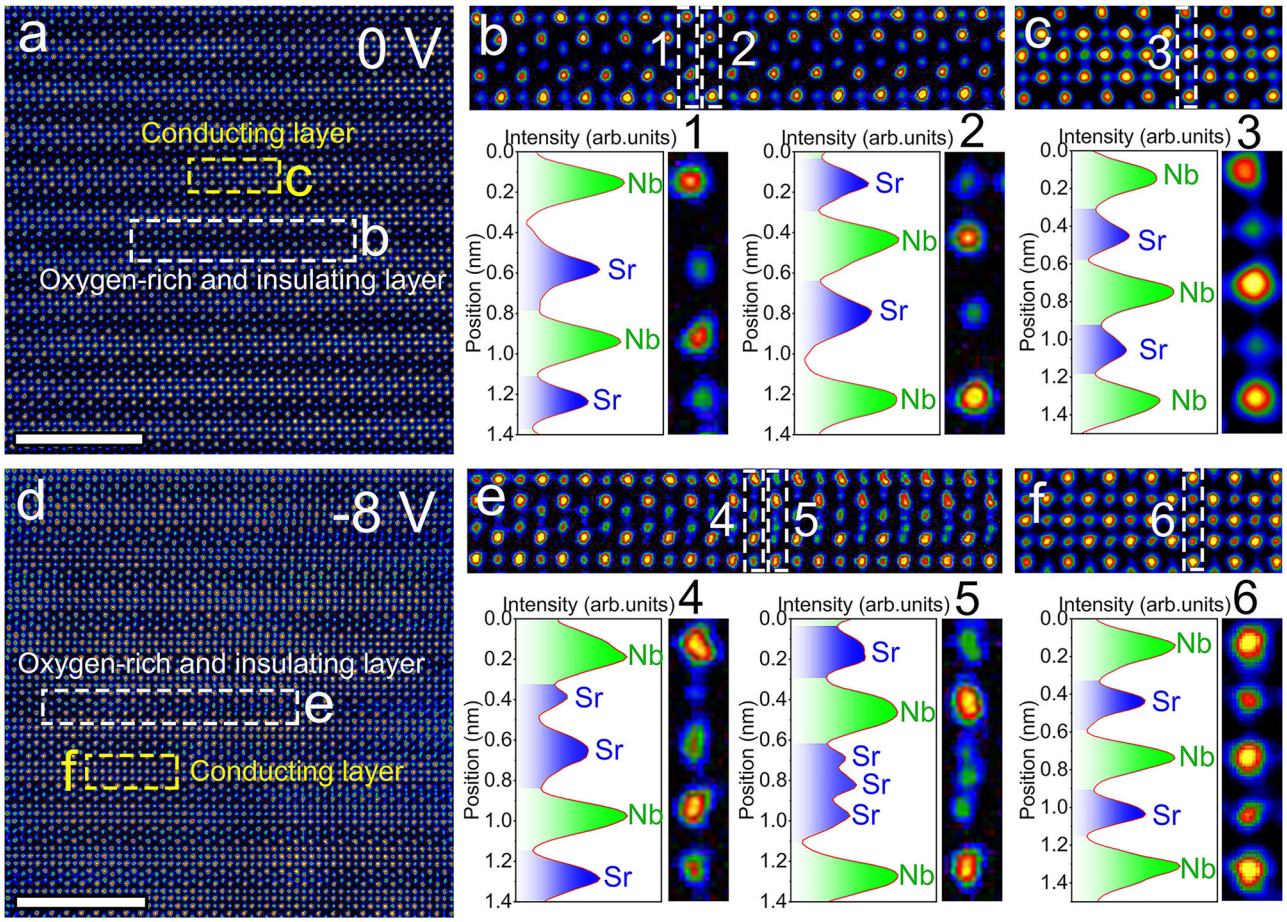

Fig. 2 | The in-situ electrical STEM studies of the NSTO/SNO/W device. a The high-resolution HAADF image of the original high-resistance state of SNO. Scale bar = 5 nm. **b** The enlarged image of the area with a dotted white rectangular box (oxygen-rich layer) in (**a**) and the line profiles. **c** The enlarged image of the area with a dotted yellow rectangular box (conducting layer) in (**a**) and the line profiles. **d** The high resolution HAADF image of the low resistance state after applying −8 V bias voltage. Scale bar = 5 nm. **e** The enlarged image of the area with a white dotted rectangular box (oxygen-rich layer) in (**d**) and the line profiles. **f** The enlarged image of the area with a white yellow rectangular box (conducting layer) in (**d**) and the line profiles.

orthorhombic structural framework remains stable, indicating that the structure can accommodate the presence of 1 or 2 oxygen vacancies per structural unit formula without significant destabilization. This provides direct evidence that when the number of oxygen vacancies is fewer than 3 per structural unit formula, a solid-solution-like structure containing oxygen vacancies is formed, leading to a reduction in resistance. In the oxygen-vacancy solid-solution structure (OVSS), oxygen vacancies are predominantly generated within the oxygen-rich and dielectric layers of the structure. Meanwhile, the structure can be recovered to the original structure after RESET in the first few cycles, showing robust reversibility of the creation and annihilation of oxygen vacancies in the OVSS.

However, after a few cycles, the NSTO/SNO/W devices show a quickly degraded stability, as the LRS cannot be steadily held soon after the SET process (as shown in Supplementary Fig. 4b and Fig. 4a, b). The instability primarily stems from the tendency of oxygen anions that migrate out of the SNO film during the SET process to readily return to the film afterward, as indicated by the red arrow in Fig. 4b. To investigate the origin of cycling instability, we analyzed the microstructure and oxygen vacancy distribution in a device cycled 100 times. The analysis revealed a distinct defective structure with pronounced lattice distortion in the interface region near the top electrode (Fig. 4c and Supplementary Fig. 18a, b). Through EELS measurement of the cycled film (Supplementary Fig. 19), the peak intensity ratio a/b gradually increased from the interface region near the top electrode to the interior (Area 1 to Area 6) of the film. This indicates that more oxygen is lost in the edge area of the film. The oxygen content of the top electrode W increased significantly after the cycle (Supplementary Fig. 18c, d). It is indicated that the oxygen lost by SNO has entered the W electrode. Quantitative analysis reveals that the defective structure contains over 3 oxygen vacancies per structural unit formula, as visualized in Fig. 4d–g (enlarged views of regions marked by white rectangles, with vacancy density mapped via heatmaps). Again, a direct correlation emerges between vacancy concentration and the magnitude of lattice distortion. STEM imaging of the device in its RESET state (Fig. 4c) demonstrates that the defective structure with excessive vacancies (>3 per structural unit formula) retains its distorted configuration rather than reverting to the pristine SNO lattice (in RESET). Nudged elastic band (NEB) simulations were performed to quantify oxygen-ion migration barriers. The calculated migration barriers for systems with 1 and 3 oxygen vacancies are 2.17 eV and 1.91 eV, respectively (Supplementary Fig. 20a, b). These results reveal that the migration barrier decreases with increasing oxygen vacancy concentration, facilitating rapid back-migration of oxygen ions from the interface to the SNO film in the post-SET stage. Consequently, the defective structure formed at the electrode-SNO interface, which remains irrecoverable during RESET, serves as a low-energy pathway for accelerated oxygen-ion diffusion, which prevents sustained retention of the LRS, as evidenced by the resistance drift marked by the red arrow in Fig. 4b.

Structural evolution under increased oxygen vacancies was further investigated. When oxygen vacancies reach 3 per structural unit

https://doi.org/10.1038/s41467-026-71912-z

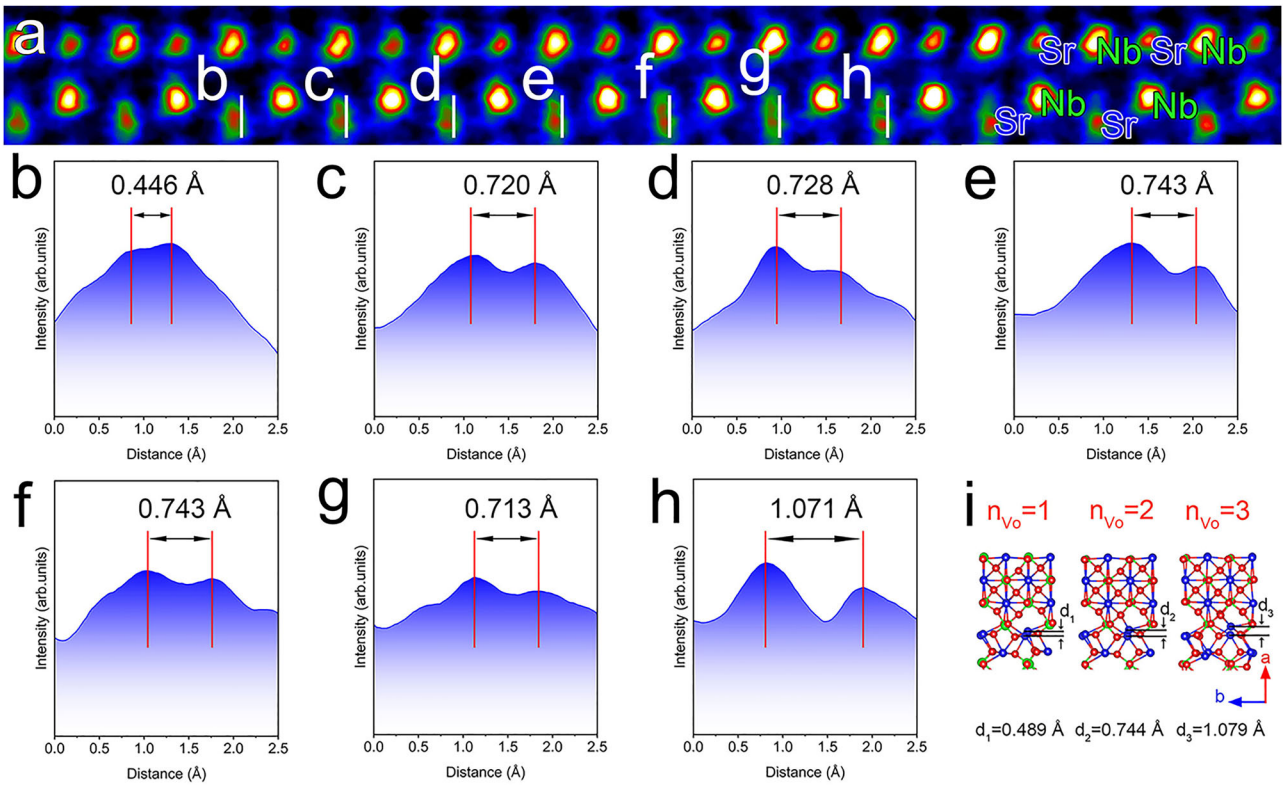

Fig. 3 | Quantization of the deviation distance of Sr atoms. a The HAADF image of Sr atomic deviation. **b**–**h** The line profiles of the Sr atom corresponding to the white line marked areas along the a-axis in (**a**). **i** The deviation of Sr atoms caused by one, two, and three oxygen vacancies calculated by DFT.

formula, a large shift in the Nb position is observed (Supplementary Fig. 21), marking an intermediate transition state toward the metallic $SrNbO_3$ phase (with a lattice parameter of $a = 4.024$ Å and space group $Pm\bar{3}m$). At 4 oxygen vacancies per structural unit formula, a pronounced Sr displacement of 1.4 Å leads to an equidistant arrangement of Sr and Nb atoms (Supplementary Fig. 21g, h), resembling the cubic structure more closely. These findings demonstrate that increasing oxygen vacancies beyond this threshold could trigger a phase transformation from the orthorhombic to the metallic cubic phase. The phase transition induced by a high density of oxygen vacancies has been observed under an elevated voltage condition (-18 V in in-situ experiments). This transformation occurs preferentially near the SNO/electrode interface and surface regions (Supplementary Fig. 22a–f). By adjusting the focus of the HAADF-STEM images (Supplementary Fig. 22g–i), we confirm that the bulk retains the original orthorhombic structure (Supplementary Fig. 22g), while the surface undergoes a structural transition to the metallic phase (Supplementary Fig. 22h). The phase transition correlates with a sharp resistance decrease observed in in-situ electrical measurements (Supplementary Fig. 23). The excessive loss of oxygen and the subsequent phase transformation drive an enhanced On/Off ratio, consistent with device performance data (Supplementary Fig. 24). However, the stability of the metallic phase impedes the reverse reaction ($5\ SrNbO_3 + O_2 \rightarrow Sr_5Nb_5O_{17}$), ultimately compromising the cycling stability of NSTO/SNO/W devices (as shown in Supplementary Fig. 24).

Once the metallic cubic phase (or defective structure) propagates as a continuous filament through the entire SNO film, the device fails, entering a permanent LRS (Supplementary Fig. 22h). This explains that, in contrast to the instability issue where maintaining the LRS is challenging, device failure caused by extended cycling or overvoltage) results in a permanent LRS. Our observations show that oxygen loss in SNO films is the primary driver of structural and functional degradation. Similar shortcoming of poor retention has been commonly observed in monolayer oxide memristors[35–38]. One effective strategy to address this issue is to limit the number of oxygen vacancies injected into the functional layer during SET. However, this approach may impose a limitation on the achievable ON/OFF ratio of the device. Another approach to enhance the reversibility of the electrochemical reactions is to prevent the enrichment of active oxygen anions at the SNO/W interface during cycling (to reduce the heterogeneous nucleation of the defective structure and extend the application of solid-state structure). This can be achieved by ensuring that the layer in direct contact with the functional film (SNO) can store oxygen anions under the applied voltage and release them under the opposite voltage.

Improving cycle stability with an oxygen reservoir

Thus, to improve the performance of the SNO memristor with poor cycle repeatability, a layer of amorphous $SrNbO_3$ (A-SNO) is added at the oxide/top electrode interface as an oxygen reservoir. In devices lacking an oxygen reservoir, the W electrode functions as an irreversible oxygen sink. During operation, oxygen ions migrate into the W electrode, forming stable WO_x, leading to progressive oxygen depletion in the functional crystalline SNO (C-SNO) layer and consequent device degradation. To mitigate this, an A-SNO oxygen reservoir layer is inserted. Its disordered structure and high density of defect sites allow it to accommodate and reversibly exchange oxygen ions with the C-SNO layer. This mechanism maintains a stable oxygen concentration gradient at the C-SNO/A-SNO interface, which is critical for cycling endurance. Direct evidence for this interfacial oxygen exchange is provided by EDS analysis (Supplementary Fig. 25), which shows a distinct increase in the oxygen gradient at this interface after cycling. Figure 5a shows the structural features of the NSTO/C-SNO/A-SNO/W device. Figure 5b and c are cross-sectional EDS mappings and a high-resolution HAADF image of the device, respectively, clearly illustrating the four-layer structure. The electrical performance of the device is also studied. Figure 5d displays the I-V curve for 100 cycles, revealing a

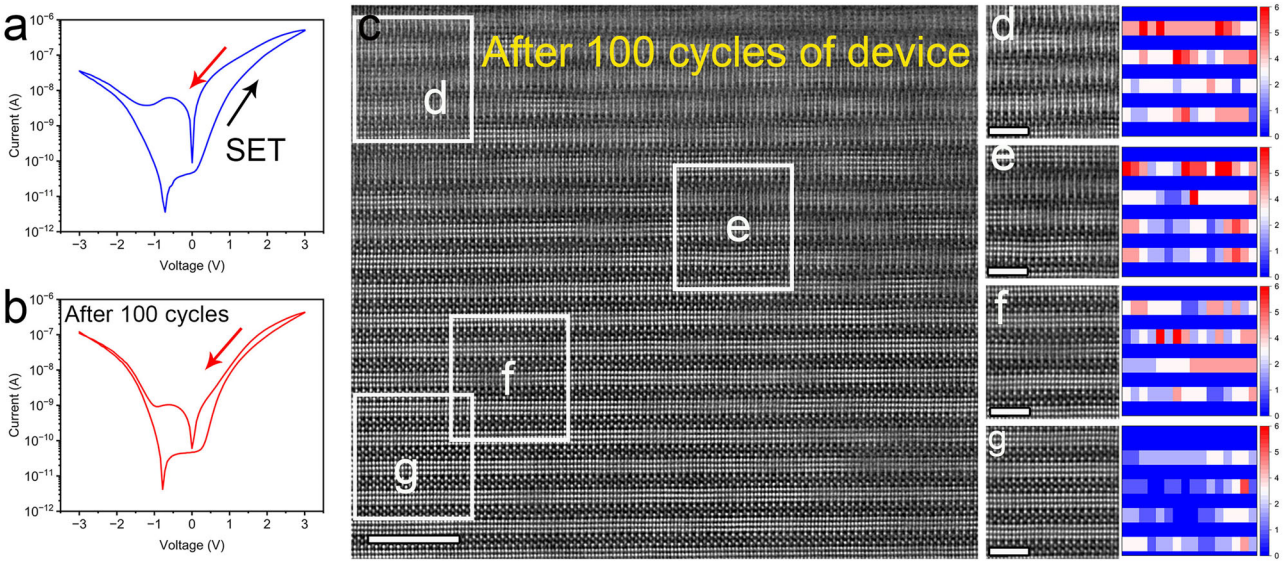

Fig. 4 | The poor retention due to oxygen loss. a The first I-V curve of the W/SNO/NSTO device. **b** The I-V curve after 100 cycles. **c** The atom-resolved HAADF image after 100 cycles of the W/SNO/NSTO device. Scale bar = 5 nm. **d**–**g** The enlarged images of the white-framed area in (**c**) and its corresponding heat map of the distribution of oxygen vacancies in the dielectric layer. Scale bar = 2 nm.

bipolar switching behavior with no significant reduction in the switching window, indicating better uniformity in the HRS/LRS. Figure 5e shows the cumulative probability of HRS and LRS at 0.72 V, which varies very little, with a minimum interval of ~40 times between HRS and LRS. The switching behavior between LRS and HRS is shown in Fig. 5f, where the HRS/LRS is highly repeatable, and the current variation is very small. The existence of a scattered distribution of oxygen vacancies is also identified by high resolution HAADF image (Supplementary Fig. 26), validating that the device is mainly running under the OVSS model (valence change mechanism), instead of the phase transition mechanism. When oxygen ions enter the amorphous SNO layer under an applied voltage, they are stored within the amorphous SNO until migrating back to the crystalline SNO film under the opposite voltage. The rate-limiting step of the reset process shifts from the oxygen-migration barrier at the SNO/W interface to the C-SNO/A-SNO interface. This transformation enhances the reversibility of oxygen vacancies, promotes the stability of oxygen vacancy solid solutions, and significantly improves the cycling stability.

To ensure robust cycling stability, the functional oxide should follow the solid-solution OVSS model, requiring oxygen vacancies to be limited to fewer than 3 per structural unit formula. In the OVSS model (Supplementary Fig. 27), the oxygen vacancies are created in SNO film during SET process: $Sr_5(Nb^{5+})_4Nb^{4+}O_{17} - xO^{2-} = Sr_5(Nb^{5+})_{4-0.4x}(Nb^{4+})_{1+0.5x}O_{17-x}$. During RESET process: $(Sr_5(Nb^{5+})_{4-0.4x}(Nb^{4+})_{1+0.5x}O_{17-x} + xO^{2-} = Sr_5(Nb^{5+})_4Nb^{4+}O_{17})$, accompanied by the redox activity of cations (Nb^{4+}/Nb^{5+} couple). When the number of oxygen vacancies reaches 3, an irreversible and defected structure forms (Supplementary Fig. 28). And when it reaches 4 per formula, the conductive cubic phase forms ($Sr_5Nb_5O_{17} = 5SrNbO_3 + O_2$, with release of O_2) (Supplementary Figs. 8b, 9f and 29). The calculated migration barriers for systems with oxygen vacancy is 1.24 eV in $SrNbO_3$ (Supplementary Fig. 14c), indicating lower energy diffusion compared to OVSS and defected structure. Both of them will degrade the cycling performance and finally break down the device, once the number of generated oxygen vacancies exceeds the critical threshold.

Applicability of the method to other materials

While we utilized $SrNbO_{3.4}$ as a model system due to its layered structure, which amplifies the lattice relaxation caused by oxygen vacancies, the core methodology is applicable to other complex oxides, including materials like $SrTiO_3$ and manganite. The fundamental principle of the method is establishing a quantitative correlation between local concentration and atomic-scale lattice distortions (specifically cation column shifts) via DFT calibration, followed by experimental verification using in-situ HAADF-STEM. In $SrTiO_3$, oxygen vacancies are known to induce lattice expansion and local symmetry breaking. As demonstrated in previous studies[9,11], clustering often leads to the formation of extended defects. The method of tracking cation displacement statistics could be adapted to $SrTiO_3$ to quantify vacancy concentrations in the pre-filamentary stage by measuring the off-centering of Ti columns[39–41], provided the STEM resolution is sufficient (sub-Angstrom). Similarly, in materials like $LaMnO_3$, the change in Mn valence state associated with migration induces a distorted structure[42]. The DFT-calibrated lattice-tracking approach can be extended to map these distortions to local oxygen stoichiometry. In metal halide perovskites ($CsPbI_3$) with anion (I^-) vacancy defects, the cations (Pb^{2+}) have also undergone displacement[43]. Therefore, the method of quantifying anion vacancies via cation displacement is also applicable to other common memristor materials.

In summary, using the established method for quantifying oxygen vacancies in SNO oxide thin films, the OVSS model is identified as an effective valence change mechanism for a device with robust performance. Once the number of injected oxygen vacancies exceeds 2, the OVSS model (valence change mechanism) is replaced by a heterogeneous defect structure/phase transition, which degrades cycling stability. Thus, NSTO/C-SNO/A-SNO/W devices are fabricated by adding an amorphous SNO layer as an oxygen reservoir, demonstrating significantly improved cyclic stability. This finding provides a clear understanding of the valence change mechanism across a wide range of oxides with potential memristive applications. Moreover, the method of quantifying anion vacancies through cation displacement can be applied to other material systems as well.

Methods

Device fabrication

SNO film was deposited by radio frequency (RF) magnetron sputtering on the conductive single-crystal Nb:$SrTiO_3$ <110> substrate with Nb doping concentration of 0.7 wt%. NSTO was chosen as the bottom

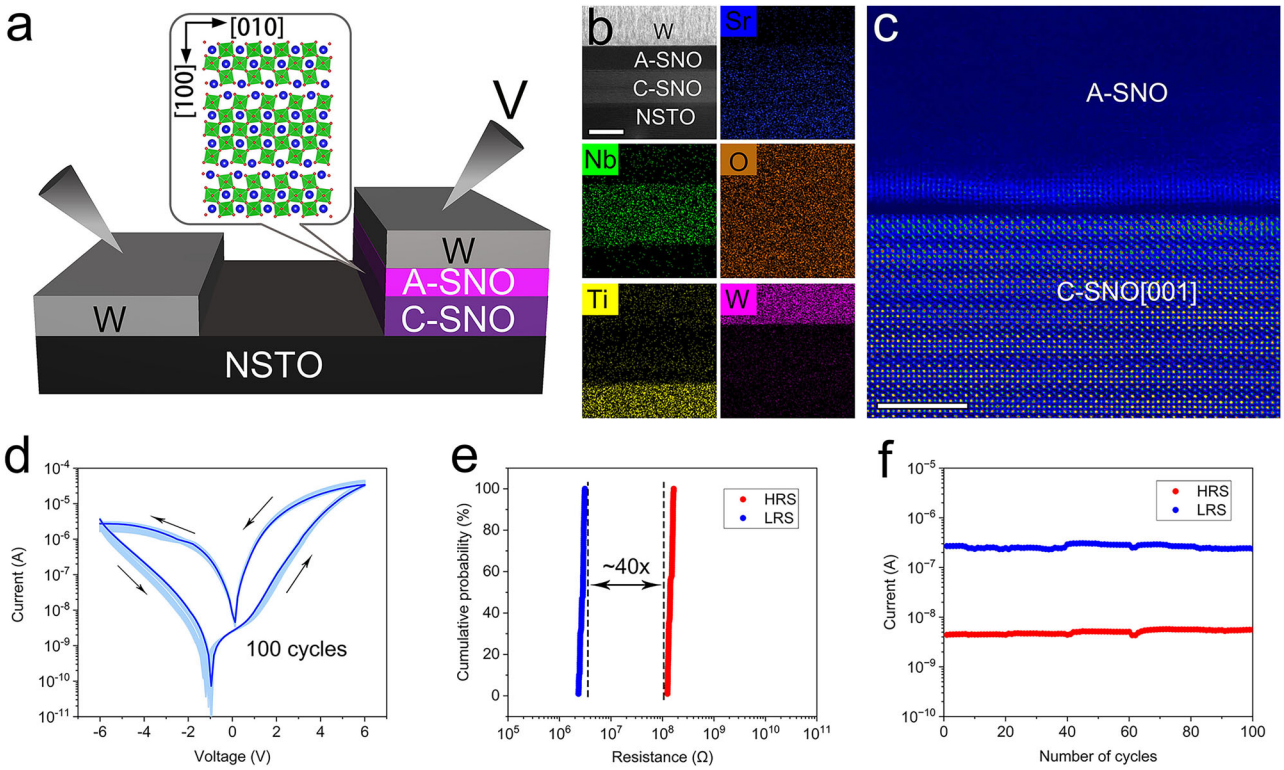

Fig. 5 | Electrical characterizations of NSTO/C-SNO/A-SNO/W memristors. a The structure schematic of the device. **b** The EDS elemental mapping images at the cross-section of the NSTO/C-SNO/A-SNO/W device. Scale bar = 50 nm. **c** The high-resolution HAADF image at the interface between the crystal and the amorphous SNO surface. Scale bar = 5 nm. **d** The I–V curves of the memristor during 100 cycles. The arrows indicate the direction of the scanning voltage. **e** The cumulative probability distribution of the resistance in HRS and LRS states. The resistances are acquired from 100 cycles at 0.72 V. **f** The endurance characteristics of the memristor undergoing over 100 SET/RESET switching cycles.

electrode because of its excellent material properties, such as metal conductivity, chemical stability, and good lattice match with SNO (Supplementary Fig. 30). Then, the SNO amorphous film was deposited on the NSTO substrate at 350 °C in an argon atmosphere of 1.4 Pa with a power of 50 W. After deposition, the film was placed in a Muffle furnace and annealed at 1200 °C for 3 h at a heating rate of 5 °C/min. Finally, W electrodes were deposited at room temperature by RF magnetron sputtering through metal masks. In addition, the NSTO/C-SNO/A-SNO/W device consists of an amorphous SrNbO3 film deposited on the SNO crystal by magnetron sputtering.

In-situ experiment and imaging

Cross-sectional TEM samples were prepared by focused ion beam (FIB) (Helios Nanolab G3 UC, FEI) for the structural characterization and in-situ STEM observation. In addition, the structure and composition of the device were characterized by double Cs-corrected TEM (Titan Themis G2 60–300, FEI) combined with EDS. The in-situ experiments were carried out using a nanochip electrical and thermal holder (Lighting, Dens solutions). The in-situ STEM sample was papered by FIB and transferred to a nanochip with the ability to measure and create biasing.

Computational details

First-principles calculations were performed using the Vienna Ab Initio Simulation Package (VASP)[44] with a plane-wave pseudopotential method and the projected augmented wave (PAW) potential. The exchange-correlation functional was approximated by the Perdew-Burke-Ernzerhof generalized gradient approximation (GGA)[45]. A 1×2×2 supercell containing 40 Sr, 40 Nb, 136-x O, and x O vacancies was fully relaxed until the force on each atom was less than 0.03 eV/Å. A plane wave cutoff energy and an electronic energy convergence threshold were set as 500 eV and 10^{-6} eV, respectively.

The energy barrier for oxygen vacancy diffusion was calculated using the climbing image NEB method, as implemented in the VASP package[46]. An initial diffusion path was constructed by linearly interpolating atomic coordinates between the initial and final states. This path subsequently underwent relaxation until the forces acting on every atom converged to below 0.05 eV/Å.

To quantitatively interpret the experimental HAADF-STEM results, theoretical image simulations were performed using the QSTEM software package[47]. These simulations were based on the rigorous multislice algorithm, which accounts for multiple scattering effects of the electron beam as it propagates through the specimen.

Electrical measurements

The B1500 semiconductor parameter analyzer with a probe station is used to measure device I-V characteristics. The W electrode applies a bias voltage to the top electrode, and the NSTO substrate serves as the bottom electrode and is grounded.

Data availability

All data are available in the main Article and Supplementary Information, or from the corresponding author upon request. Source data are provided with this paper.

References

1. Waser, R. et al. Redox-based resistive switching memories – nanoionic mechanisms, prospects, and challenges. *Adv. Mater.* **21**, 2632–2663 (2009).

2. Kwon, D.-H. et al. Atomic structure of conducting nanofilaments in TiO_2 resistive switching memory. *Nat. Nanotechnol.* **5**, 148–153 (2010).
3. Yang, J. J., Strukov, D. B. & Stewart, D. R. Memristive devices for computing. *Nat Nanotechnol* **8**, 13–24 (2012).
4. Wedig, A. et al. Nanoscale cation motion in TaO_x, HfO_x and TiO_x memristive systems. *Nat. Nanotechnol.* **11**, 67–74 (2015).
5. Meijer, G. I. Who Wins the nonvolatile memory race? *Science* **319**, 1625–1626 (2008).
6. Luo, Q., et al. 8-layers 3D vertical RRAM with excellent scalability towards storage class memory applications. *IEEE International Electron Devices Meeting (IEDM)*. 2.7.1-2.7.4 (2017).
7. Feng, W. et al. Investigation of switching mechanism in HfO_x-ReRAM under low power and conventional operation modes. *Sci. Rep.* **6**, 39510 (2016).
8. Heisig, T. et al. Oxygen exchange processes between oxide memristive devices and water molecules. *Adv. Mater.* **30**, e1800957 (2018).
9. Cooper, D. et al. Anomalous resistance hysteresis in oxide ReRAM: oxygen evolution and reincorporation revealed by in situ TEM. *Adv. Mater*. **29**, 10.1002/adma.201700212 (2017).
10. Shen, W. et al. Improved endurance behavior of resistive switching in (Ba,Sr)TiO_3 thin films with W top electrode. *Appl. Phys. Lett*. **93**, https://doi.org/10.1063/1.3039809 (2008).
11. Du, H. et al. Nanosized conducting filaments formed by atomic-scale defects in redox-based resistive switching memories. *Chem. Mater*. **29**, 3164–3173 (2017).
12. Baeumer, C. et al. Spectromicroscopic insights for rational design of redox-based memristive devices. *Nat. Commun.* **6**, 8610 (2015).
13. Li, Y. et al. Ag-doped non–imperfection-enabled uniform memristive neuromorphic device based on van der Waals indium phosphorus sulfide. *Sci. Adv.* **10**, eadk9474 (2024).
14. Hus, S. M. et al. Observation of single-defect memristor in an MoS_2 atomic sheet. *Nat. Nanotechnol.* **16**, 58–62 (2021).
15. Lei, P. et al. High-performance memristor based on 2D layered bioi nanosheet for low-power artificial optoelectronic synapses. *Adv. Funct. Mater*. **32**, https://doi.org/10.1002/adfm.202201276 (2022).
16. Wang, Y. et al. Achieving adjustable digital-to-analog conversion in memristors with embedded $Cs_2AgSbBr_6$ nanoparticles. *Nanoscale* **15**, 7344–7351 (2023).
17. Sawa, A. Resistive switching in transition metal oxides. *Mater. Today*. **11**, 28–36 (2008).
18. Tokura, Y. & Nagaosa, N. Orbital physics in transition-metal oxides. *Science* **288**, 462–468 (2000).
19. Takagi, H. & Hwang, H. Y. An emergent change of phase for electronics. *Science* **327**, 1601–1602 (2010).
20. Janousch, M. et al. Role of oxygen vacancies in Cr-doped $SrTiO_3$ for resistance-change memory. *Adv. Mater*. **19**, 2232–2235 (2007).
21. Shibuya, K. et al. Impact of defect distribution on resistive switching characteristics of Sr_2TiO_4 thin films. *Adv. Mater*. **22**, 411–414 (2010).
22. Yang, J. J. et al. Memristive switching mechanism for metal/oxide/metal nanodevices. *Nat. Nanotechnol.* **3**, 429–433 (2008).
23. Dong, R. et al. Electrically Triggered Domain Wall Movement in Cu_2Se Semiconductor. *ACS Appl. Mater. Interfaces*. **16**, 15525–15532 (2024).
24. Bai, H. et al. Electroresistance in multipolar antiferroelectric Cu_2Se semiconductor. *Nat. Commun*. **12**, 7207 (2021).
25. Bai, H. et al. Electrically tunable antiferroelectric to paraelectric switching in a semiconductor. *Nano Lett* **22**, 4083–4089 (2022).
26. Wang, H. et al. Unraveling the reaction mechanisms of electrode materials for sodium-ion and potassium-ion batteries by in situ transmission electron microscopy. *IM* **1**, 196–212 (2022).
27. Chen, C. et al. Patterning oxide nanopillars at the atomic scale by phase transformation. *Nano Lett* **15**, 6469–6474 (2015).
28. Lichtenberg, F. et al. Synthesis of perovskite-related layered $A_nB_nO_{3n+2}$=ABO_X type niobates and titanates and study of their structural, electric and magnetic properties. *Prog. Solid State Chem*. **29**, 1–70 (2001).
29. Isawa, K. et al. Synthesis and transport properties of Sr_xNbO_3(0.75≤x≤0.90). *PRB*. **47**, 2849–2853 (1993).
30. Kuntscher, C. A. et al. Extremely small energy gap in the quasi-one-dimensional conducting chain compound $SrNbO_{3.41}$. *Phys. Rev. Lett*. **89**, 10.1103/PhysRevLett.89.236403 (2002).
31. Kobayashi, W. et al. Anisotropic thermoelectric properties associated with dimensional crossover in quasi-one-dimensional $SrNbO_{3.4+d}$(d~0.03). *PRB*, **84**, https://doi.org/10.1103/PhysRevB.84.085118 (2011).
32. Chen, C. et al. Atomic-scale origin of the quasi-one-dimensional metallic conductivity in strontium niobates with perovskite-related layered structures. *ACS Nano* **11**, 12519–12525 (2017).
33. Yao, T. et al. Ferroelectric oxide thin film with an out-of-plane electrical conductivity. *Nano Lett* **20**, 1047–1053 (2020).
34. Li, C. et al. Atomic scale characterization of point and extended defects in niobate thin films. *Ultramicroscopy* **203**, 82–87 (2019).
35. Noman, M. et al. Computational investigations into the operating window for memristive devices based on homogeneous ionic motion. *APPL PHYS A-MATER* **102**, 877–883 (2011).
36. Kim, D.-W. et al. Doping-level Dependences of switching speeds and the retention characteristics of resistive switching Pt/$SrTiO_3$ junctions. *J KOREAN PHYS SOC* **57**, 1432–1436 (2010).
37. Raab, N., Bäumer, C. & Dittmann, R. Impact of the cation-stoichiometry on the resistive switching and data retention of $SrTiO_3$ thin films. *AIP Adv*. **5**, https://doi.org/10.1063/1.4919697 (2015).
38. Yang, M. et al. Direct evidence of filamentary resistive switching in Pt/Nb-doped $SrTiO_3$ junctions. *J.Appl. Phys*. **115**, https://doi.org/10.1063/1.4870867 (2014).
39. Li, T. et al. Strong room-temperature ferroelectricity in strained $SrTiO_3$ homoepitaxial film. *Adv. Mater*. **33**, 10.1002/adma.202008316 (2021).
40. Chen, C. et al. Defect and strain engineering coenhanced nanoscale ferroelectricity in $SrTiO_3$ thin films. *ACS Nano* **19**, 13479–13488 (2025).
41. Li, T. et al. Superfine nanodomain engineering unleashing ferroelectricity in incipient ferroelectrics. *J.Am.Chem.Soc*. **146**, 20205–20212 (2024).
42. Ricca C., Niederhauser N., Aschauer U. Local polarization in oxygen-deficient $LaMnO_3$ induced by charge localization in the Jahn-Teller distorted structure. *Phys. Rev. Res*. **2**, https://doi.org/10.48550/arXiv.2002.09921 (2020).
43. Woo, Y. W. et al. Inhomogeneous defect distribution in mixed-polytype metal halide perovskites. *ACS Energy Lett* **8**, 356–360 (2022).
44. Kresse, G. & Hafner, J. Ab initio molecular dynamics for open-shell transition metals. *PRB* **48**, 13115–13118 (1993).
45. Blöchl, P. E. Projector augmented-wave method. *PRB* **50**, 17953–17979 (1994).
46. Henkelman, G., Uberuaga, B. P. & Jónsson, H. A climbing image nudged elastic band method for finding saddle points and minimum energy paths. *J. Chem. Phys*. **113**, 9901–9904 (2000).
47. Koch, C. T. Determination of core structure periodicity and point defect density along dislocations. Arizona State University, https://ui.adsabs.harvard.edu/abs/2002PhDT.....50K/abstract (2002).

Acknowledgements

This work was supported by the National Key R&D Program of China (2024YFE029300) and the National Natural Science Foundation of China (52573254, 52150710537).

Author contributions

Under the guidance of J.W., Z.W. designed and conducted the experiment and wrote the initial draft. W.L. carried out the theoretical calculations and provided relevant explanations. Y.L., M.W., A.G., and H.L. assisted in the transmission electron microscopy characterization. X.S., L.J., C.C., W.Z., and HG.L. made revisions to the manuscript. R.E.D.-B and J.W. were responsible for project supervision.

Competing interests

The authors declare no competing interests.

Additional information

Supplementary information The online version contains supplementary material available at https://doi.org/10.1038/s41467-026-71912-z.

Correspondence and requests for materials should be addressed to Rafal E. Dunin-Borkowski or Jinsong Wu.

Peer review information *Nature Communications* thanks Regina Dittmann and the other anonymous reviewer(s) for their contribution to the peer review of this work. A peer review file is available.